Size-limited high-density nanopore formation in two-dimensional moiré materials

Philipp Valerius,[1] Carsten Speckmann,[1] Boris V. Senkovskiy,[1] Alexander Grüneis,[1] Nicolae Atodiresei,[2] and Thomas Michely[1,*]

[1]*II. Physikalisches Institut, Universität zu Köln, Zülpicher Straße 77, 50937 Köln, Germany*

[2]*Peter Grünberg Institute and Institute for Advanced Simulation, Forschungszentrum Jülich, Wilhelm-Johnen-Straße,52428 Jülich, Germany*

(Received 8 March 2022; revised 28 April 2022; accepted 28 April 2022; published 9 May 2022)

Patterns formed in monolayer graphene (Gr) and hexagonal boron nitride (h-BN) upon ion irradiation in the temperature range from 950 to 1530 K using 500 eV He^+ at normal or 500 eV Xe^+ at grazing incidence and fluences up to 2.5×10^{19} ions/m^2 are investigated by room-temperature scanning tunneling microscopy. Subnanometer pores are created and are distributed with the periodicity of the moiré which results from the interaction of the monolayers with their Ir(111) substrate. The moiŕe contains trapping sites for vacancies within each moiré unit cell as is investigated in detail for the case of h-BN with the help of *ab initio* calculations. The density of the nanopores is extremely high in the order of 10^{17} pores/m^2 and their size distribution is limited by the size of the vacancy traps causing excess vacancies to be expelled from the array and to anneal at preexistent defects. Successful delamination of a perforated Gr monolayer from the substrate is demonstrated and makes the material accessible for membrane research.

DOI: 10.1103/PhysRevB.105.205413

I. INTRODUCTION

Transport of gases and liquids through nanoporous atomically thin membranes like graphene (Gr) is a viable and dynamic area of research. The variability of the pore size from the subnanometer range [1–3] to tens of nanometers [4,5] together with the inherent high-membrane permeance hold potential for a wide range of applications including water desalination [6–8], gas purification [4], and separation of miscible liquids [3].

Aside from their natural occurence as defects [9], nanopores can be created by electron and ion irradiation often combined with chemical methods [1–5,7,8,10]. Generally, these methods create pores randomly in space with broad size distributions. This is due to the inherent randomness of energy deposition, nucleation, and subsequent growth [3]. Randomness in location and size limit permeance and selectivity since fewer nanopores of the proper size per unit area are available. Such disadvantages can be overcome in a top-down approach involving direct writing with focused beams [1,4,11,12], however, at the expense of inherent slowness and lack of scalability.

One way to improve size regularity and density of the nanopores is to use template effects. Examples are self-organized films of block copolymers [5] or nanoporous silica [8] on Gr as masks for reactive ion etching and the use of substrate moirés for templating. The moiré effect was used to create nanopores in hexagonal boron nitride (h-BN) monolayers on Rh(111), where room-temperature ion irradiation resulted in well-defined pores of 2-nm diameter, though still sparsely positioned [13,14]. These hBN sheets with pores could even be transferred to foreign substrates [14]. For Gr and h-BN on Ir(111), room-temperature irradiation and annealing resulted in dense networks of nanopores defined by the moiré periodicity. However, the size distribution had long tails to large sizes in the case of h-BN monolayers [15] or an only limited order in the case of Gr [16,17].

This paper is devoted to a systematic study on the formation of dense nanopore arrays (density $\approx 10^{17}$ nanopores/m^2) in the subnanometer range (average diameter 0.6–0.7 nm) using the moiré template provided by placing a monolayer of h-BN or Gr on Ir(111) [18,19]. Instead of using large energy deposition in single impacts at room temperature and annealing at elevated temperature to form nanopores (vacancy clusters are used synonymously in the following) [15–17], here we tune to a regime where the description of the processes is more simple: we use ion impacts that create at most a single vacancy in the monolayer two-dimensional (2D) material and irradiation is conducted at elevated temperature lifting the distinction between damage and annealing phase. Thus, the process of vacancy cluster formation reduces to the migration and aggregation of single vacancies in an inhomogeneous potential energy landscape defined by the moiré. Under these conditions, highly regular arrays of vacancy clusters result for the h-BN monolayer on Ir(111). The formation of these vacancy clusters is analyzed with the help of density functional theory (DFT) calculations.

The most striking result of our investigation is a self-limitation of nanopore growth during high-temperature ion irradiation: once a critical subnanometer size of the nanopores is reached during irradiation, the growth of nanopores stops. Instead of diffusing just a few nanometers to reach the nearest

*michely@ph2.uni-koeln.de

 ©2022 American Physical Society

trapping site of a moiré unit cell, the vacancies created start to move hundreds of nanometers to anneal or heterogeneously nucleate at preexisting defects.

II. METHODS

The experiments were conducted in an ultrahigh vacuum system (base pressure in the 10^{-11}-mbar range) equipped with variable temperature scanning tunneling microscopy (STM) and low-energy electron diffraction (LEED). Ir(111) was cleaned by cycles of 1 keV Xe^+ ion irradiation and flash annealing to 1550 K. For gas exposure a dosing tube was used, giving rise to a local pressure enhancement at the sample location by a factor of ≈ 80 compared to the pressure measured by a distant ion gauge and specified here. Gr in single-crystal quality was grown on Ir(111) by adsorbing ethylene at room temperature until saturation, subsequent thermal decomposition at 1450 K, followed by exposure to 5×10^{-8} mbar ethylene for ≈180 s at the same high temperature. A monolayer of h-BN of similar quality was grown by 1×10^{-8} mbar borazine exposure for ≈120 s at 1250 K sample temperature. The h-BN monolayer consists of two types of domains of mirror symmetry with respect to each other. The domains are threefold symmetric and aligned to the sixfold-symmetric Ir surface layer [18].

500 eV He^+ irradiation was performed at normal incidence, while 500 eV Xe^+ ion exposure was conducted at the grazing angle of 75° with respect to the surface normal. The ion flux was adjusted by a Faraday cup moved to the sample location prior to each irradiation experiment. The ion fluence was set by the irradiation time at the given ion flux. The elevated sample temperature during irradiation is controlled by a thermocouple and specified for each experiment.

STM imaging was conducted at room temperature and the software WSXM was used for image analysis [20]. LEED patterns were digitally recorded over an energy range from about 20 to 150 eV.

Raman spectroscopy measurements of a detached Gr nanopore membrane were conducted under ambient conditions in a backscattering geometry using a Renishaw inVia setup, a laser with 532 nm wavelength and an optical microscope with a 100× objective of 0.85 numerical aperture. The laser was operated with a power of only 6.8 mW in order to avoid damage. The spectra were calibrated using a Si peak at 520.5 cm^{-1}.

Density functional theory (DFT) [21,22] calculations were performed by employing the VASP code [23–25] that uses pseudopotentials generated within the projector augmented wave method [26] and the generalized gradient approximation [27]. As a starting configuration the relaxed geometry of the (12×12) h-BN on (11×11) Ir(111) unit-cell system was used. Specific N and B atoms were removed to create vacancy clusters in the h-BN layer. The slab was modeled by three Ir atomic layers, enough to correctly describe the chemical bonding of N and B atoms with the Ir surface atoms. A plane-wave basis set with an energy cutoff of 500 eV is used for the calculations. The structural optimizations were done by Γ-point sampling of the Brillouin zone such that the calculated Hellmann-Feynman forces were smaller than 10 meV/Å. Since the van der Waals interactions are a key ingredient in the bonding of h-BN to Ir(111) [18,28], we employed the nonlocal correlation energy functional vdW-DF2 [29] that uses the exchange energy functional developed by Hamada [30]. The theoretical figures have been plotted with the VESTA [31] software.

III. RESULTS AND DISCUSSION

A. Nanopore arrays in the h-BN and Gr moirés on Ir(111)

In this section the qualitative features of vacancy cluster arrays created by high-temperature ion irradiation in h-BN or Gr on Ir(111) are introduced for the example of 500 eV He^+ ion exposure.

The STM topograph in Fig. 1(a) shows a pristine h-BN layer on Ir(111) at negative tunneling bias, where the moiré supercell with the periodicity of 2.9 nm is visible through a regular array of depressions (valleys). The moiré unit cell is indicated in the inset as a rhombus with the valley in its center. The valley atoms are chemisorbed to Ir(111), while the h-BN in the surrounding mesa is physisorbed to Ir [18]. After 500 eV He^+ irradiation with an ion fluence of 1.2×10^{19} ions/m^2 at 1200 K a vacancy cluster formed in almost every valley, while the mesa is free of vacancy clusters as shown in Fig. 1(b). In the chosen negative bias contrast the apparent depth increases from about 20 pm for a valley to about 40 pm for a valley containing a vacancy cluster as obvious from the comparison of the line profiles for unirradiated and irradiated samples in Figs. 1(a) and 1(b). Identification of vacancy clusters is more reliable at positive sample bias, where valleys without vacancy clusters appear as protrusion [compare topograph of unirradiated sample in Fig. 1(c)] with a height of about 25 pm. After irradiation [Fig. 1(d)] a vacancy cluster appears as a dark spot with a depth of about 40 pm in the center of a bright protrusion, making its identification unambiguous. The shapes of the vacancy islands are compact, circular to elongated. Due to their smallness, their convolution with the tip shape, and the contrast being determined also by electronic effects rather than geometry, it is neither possible to give a reliable estimate for their shape nor their size. In LEED patterns of the pristine h-BN layer, up to two orders of moiré reflections are visible which surround the first-order h-BN [encircled blue in Fig. 1(e)] and Ir (encircled yellow) spots. The number of visible moiré reflections decreases upon irradiation [compare Fig. 1(f)]. Consistent with the real-space view, the moiré is preserved, though its perfection has decreased.

A similar self-organization process takes place for ion irradiation of Gr on Ir(111) which forms a moiré with a periodicity of 2.5 nm and a unit cell as depicted in the inset Fig. 2(a). After irradiation with an ion fluence of 1.2×10^{19} ions/m^2 500 eV He^+ at 1150 K small vacancy clusters formed in the majority of the moiré unit cells. A characteristic separation of 2.5 nm between vacancy clusters [compare line profile of Fig. 2(b)] and some regularity in the arrangement of the vacancy clusters is apparent, but they are less accurately positioned as for h-BN/Ir(111) and do not form a two-dimensional lattice. The reason for this zwitter appearance of order and disorder is that there are two preferential vacancy cluster locations in each moiré unit cell, rather than one as for h-BN

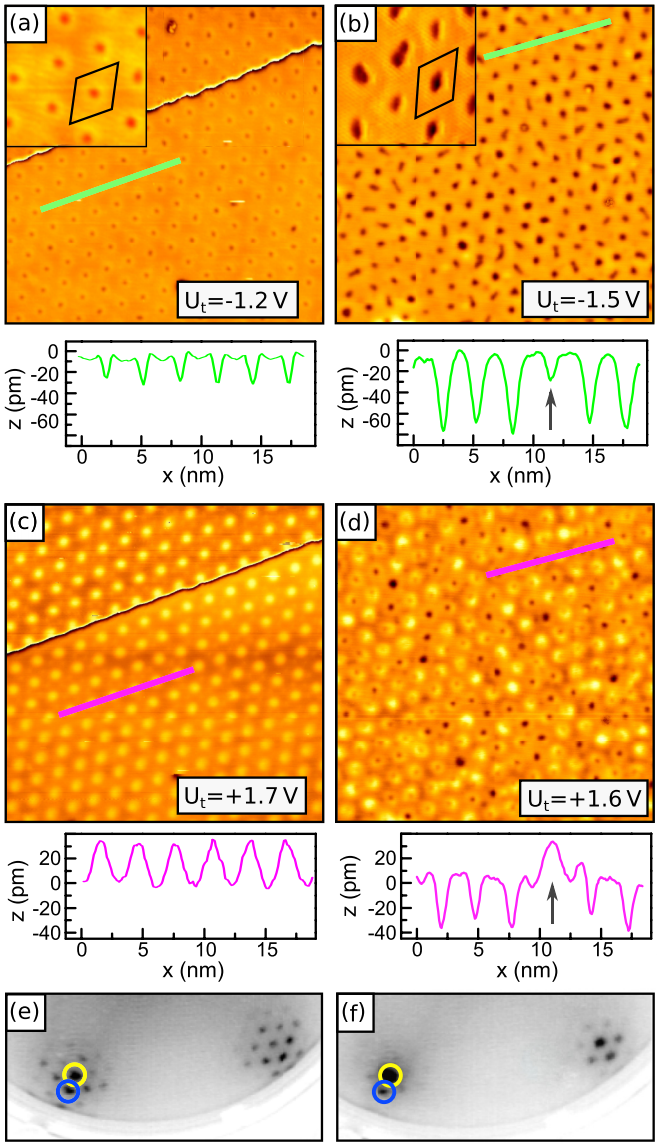

FIG. 1. Negative (a), (b) and positive (c), (d) bias contrast STM topographs with associated height profiles of unirradiated (a), (c) and irradiated h-BN/Ir(111) (b), (d). Irradiation was conducted with a fluence of 1.2×10^{19} ions/m^2 500 eV He^+ at 1200 K. Insets in (a) and (b) are magnified views with the moiré unit cell highlighted by the black rhombus. The vertical arrow in the line profiles of (b) and (d) indicates a valley without a vacancy cluster. Unirradiated (e) and irradiated (f) sample LEED patterns at 68 eV. Blue or yellow circles enclose a first-order h-BN or Ir(111) reflection, respectively. Image sizes are 45 nm × 45 nm for (a)–(d), and 9 nm × 9 nm for insets in (a) and (b). Positive and negative sample bias voltages U_s used for tunneling are indicated in (a)–(d).

Ir(111) [16]. These preferential locations are at the centers of the two triangles created by the dashed line in the unit-cell rhombus depicted in the inset of Fig. 2(a) (hcp and fcc regions in the terminology of Ref. [16]). Vacancy clusters are absent in the bright areas at the corners of the moiré unit cell (top regions). The profile in Fig. 2(a) shows that vacancy clusters are associated with depressions of up to 90 pm depth. In LEED patterns of the irradiated sample, aside from the first-order Gr

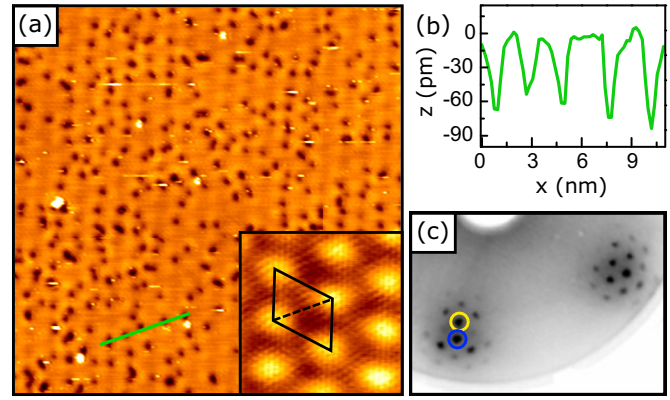

FIG. 2. (a) STM topograph and (b) associated height profile of Gr/Ir(111) irradiated by 500 eV He^+ with a fluence of 1.2×10^{19} ions/m^2 at 1150 K. Inset in (a) displays the moiré pattern of pristine Gr/Ir(111), a moiré unit cell is indicated by the black rhombus. Dashed line in rhombus divides unit cell in two triangles. Vacancy clusters are mostly located in centers of triangles, but never at their corners. (c) LEED of sample shown in (a) at 70 eV. Blue or yellow circles enclose a first-order Gr or Ir(111) spot, respectively. Image size is 45 nm × 45 nm and 8 nm × 8 nm for inset, sample bias is $U_s = -0.6$ V and $U_s = -1.3$ V for inset.

[encircled blue in Fig. 1(e)] and Ir (encircled yellow) spots, also up to two orders of surrounding moiré reflections are visible. Although inferior to the LEED pattern of an undamaged h-BN layer, it still indicates an ordered moiré.

B. Mechanism of cluster array formation

Vacancy cluster formation in the moiré of h-BN with Ir(111) at 1200 K requires the creation of vacancies in the h-BN monolayer. Based on the small nuclear charge of He, B, and N atoms, the scattering cross section of impinging He ions will be small implying little damage per ion. Consistent with this reasoning, below we obtain an experimental estimate for the sputtering yield of $Y_{\text{h-BN}} \approx 0.25$, i.e., 0.25 B and N atoms are removed per impinging He^+ ion in average. This value is consistent with estimates obtained with Monte Carlo simulations in the binary collision approximation [32]. In conclusion, per impact at most a single missing atom in the h-BN layer is created. The experiments presented here were in fact tuned on purpose to the single-vacancy sputtering regime in order to avoid complications in the interpretation that would result from impacts giving rise to complex damage patterns and the direct creation of vacancy clusters of varying size.

The arrangement of vacancies into clusters, with one cluster in each moiré unit cell, implies immediately the mobility of single B and N vacancies within the h-BN layer at 1200 K, the temperature of ion exposure. Based on the DFT calculations by Zobelli *et al.* [33] vacancy migration barriers are $\Delta E = 2.6$ eV for a B and $\Delta E = 5.8$ eV for an N vacancy in freestanding h-BN monolayers. More recent calculations by Weston *et al.* [34] yield values of $\Delta E = 2.8$ and 5.0 eV, respectively, in reasonable agreement with the previous calculations. Based on these numbers and the universal Arrhenius law for thermally activated diffusion $\nu = \nu_0 e^{\frac{-\Delta E}{k_B T}}$, nitrogen vacancy migration at 1200 K can be ruled out for the freestand-

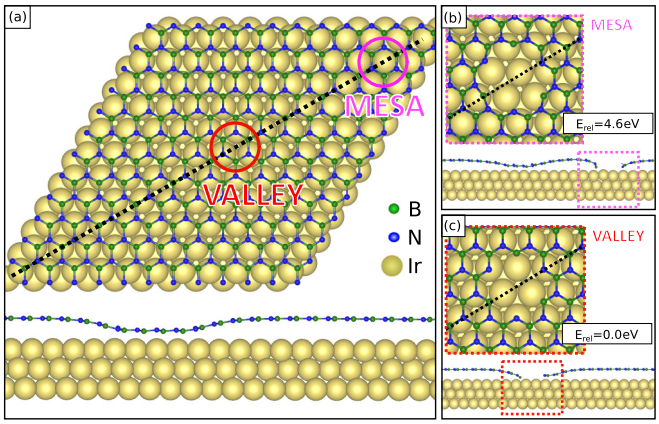

FIG. 3. (a) Top view and side view ball models of the DFT moiré supercell for h-BN on Ir(111). The supercell consists of (12 × 12) h-BN on (11 × 11) Ir(111) unit cells. The side view is along the dashed black line in the top view. (b) Magnified top view ball model of DFT calculation for the moiré supercell with a vacancy cluster consisting of three missing N and three missing B atoms in the mesa region. The location of the vacancy cluster is indicated in (a) through a purple circle. The side view of the entire unit cell with vacancy cluster is taken along the black dashed line. (c) As (b), but with vacancy cluster located in the valley region. The location of the vacancy cluster is indicated in (a) through a red circle. Relative formation energies E_{rel} of the vacancy clusters are indicated in (b) and (c).

ing monolayer. Here ν is the vacancy hopping rate, ν_0 an attempt frequency in the order of 10^{13} s^{-1} defined by typical lattice vibration frequencies, k_B the Boltzmann constant, and T the temperature. We conclude that vacancy migration is assisted, either by the many impinging ions that just transfer energy and do not sputter, or through the substrate. While the former cannot be excluded, the latter will be shown below to hold.

The observation of the vacancy cluster positioning precisely within the valley areas must be an effect of a strong energetic preference for this location. Insight into the energetics of vacancy cluster positioning is provided through density functional theory (DFT) calculations for h-BN/Ir(111) of which examples are shown in Fig. 3. Figure 3(a) displays the moiré unit cell without any vacancy cluster [18]. It is apparent that the positions of the B and N atoms vary laterally over the unit cell. In the central area, where the N atoms sit atop of the Ir atoms and the B atoms in threefold hollow sites, h-BN is chemisorbed to Ir, while in the other areas it is only physisorbed. This becomes obvious through the side view of the unit cell along the diagonal indicated by a black dashed line in Fig. 3(a). In the central valley region, the B and N atoms are close to the Ir(111) surface plane due to the chemisorption (distance ≈2.2 Å), while in all other areas, i.e., in the mesa, they are in a rather uniform and much greater height (distance ≈3.5 Å) [18].

A situation with an example vacancy cluster in the mesa, consisting of three missing B and three missing N atoms, is depicted in Fig. 3(b). The top view makes plain that the edge atoms bounding the newly created vacancy cluster rearrange laterally to compensate for their missing bonding partners. In the side view it becomes obvious that edge atoms also moved down in order to form compensating bonds with the Ir substrate. Thereby they cause a substantial vertical deformation of the h-BN layer in the vacancy cluster surrounding and drag nearby atoms down. This downward movement implies an energy penalty for the fully coordinated atoms next to the edge. The height of the atoms in the mesa was determined by the equilibrium of van der Waals attraction and Pauli repulsion. As atoms next to the edge are dragged down by the vacancy cluster edge atoms binding to Ir, substantial repulsive forces are acting on them.

To the contrary, there is little change in the h-BN layer next to the vacancy cluster, when the cluster is placed in the valley as shown in Fig. 3(c). The cluster edge atoms had already strong chemical bonds with the Ir substrate prior to cluster atom removal. Little extra deformation is introduced into the h-BN sheet by vacancy cluster formation. Consequently, the formation energy of the cluster is 4.6 eV lower in the valley compared to the mesa. This large energy difference implies that even at 1200 K and in the absence of additional barriers, such a cluster would never move away from the valley onto the mesa: a Boltzmann factor estimate implies a negligible occupation probability of mesa sites. In consequence, also clusters in neighboring moiré unit cells are unable to merge at 1200 K.

It is evident that these conclusions are not limited to a specific cluster size, but should hold as long as the cluster fits into the chemisorbed valley area, i.e., as long as it is smaller than ≈20 vacancies. We tested also less symmetric clusters and found for a vacancy cluster composed of six missing N and three missing B atoms an energetic preference of 6.2 eV for the valley compared to the mesa.

A similar mechanism holds for small vacancy clusters in Gr/Ir(111) with the difference that within the moiré unit cell a specific region is strongly *disfavored* for positioning small vacancy clusters [16]. This region is the top region which is bright in the inset of Fig. 2(a). Formation of a vacancy cluster with four missing carbon atoms in the top region is disfavored by about 4 eV with respect to the two other high-symmetry regions in the moiré unit cell, which have have similar formation energies. This ambiguity explains the less perfect order of vacancy clusters in Gr, as observed in Fig. 2(a).

C. Nanopore growth stagnation

Aside from preferential nucleation of nanopores at specific locations in the moiré, a second remarkable feature of these vacancy cluster arrays becomes obvious when analyzing their evolution with ion fluence. We start with the h-BN/Ir(111) case.

Figure 4(a) displays as full red dots the fluence dependence of the vacancy cluster number density n measured in vacancy clusters per moiré unit cell. It is apparent that n gradually increases and approaches unity for fluences above 1×10^{19} ions/m^2. The insets of Figs. 4(b) and 4(c) show the vacancy clusters in the arrays for unsaturated n after a fluence of 0.30×10^{19} ions/m^2 500 eV He$^+$ and almost saturated n after a fluence of 1.20×10^{19} ions/m^2, respectively.

The large-scale topographs of Figs. 4(b) and 4(c) display an additional feature: while in the topograph of Fig. 4(b) the h-BN layer perforated by vacancy clusters still extends over

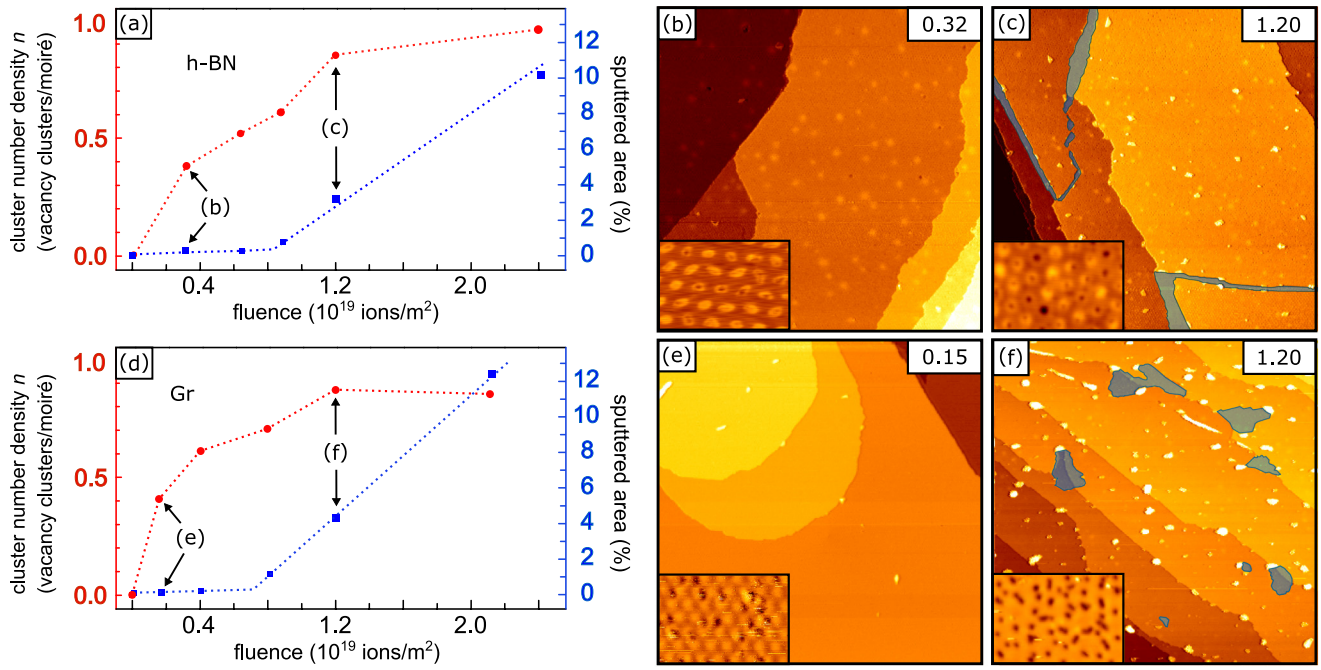

FIG. 4. (a) Dependence of vacancy cluster number density n and sputter removed area in h-BN on Ir(111) on 500 eV He^+ ion fluence at 1200 K. Full red dots and left axis: n in clusters per moiré cell; full blue squares and right y axis: removed h-BN layer area by sputtering (excluding cluster area). Lines to guide the eye. (b), (c) STM topographs taken after ion fluences as indicated in (a) and in the top right corners in units of 10^{19} ions/m^2. (d) Same as (a), but for Gr on Ir(111) and at 1150 K irradiation temperature. (e), (f) STM topographs taken after ion fluences as indicated in (d). Insets in STM topographs are magnified views. Removed areas in (c) and (f) are shaded blue. See Figs. S1 and S2 of Ref. [35] for STM topographs of additional fluences and without coloring of sputtered areas. Topograph sizes are 350 nm × 350 nm, 12 nm × 17 nm for insets of (b), (c), and 15 nm × 21 nm for insets of (e), (f). Sample bias is in (b) $U_s = -1.4$ V and for inset $U_s = +1.4$ V, in (c) $U_s = -1.3$ V and for inset $U_s = +1.5$ V, in (e) $U_s = -1.4$ V and for inset $U_s = -0.8$ V, and in (f) $U_s = -1.6$ V and for inset $U_s = -1.8$ V.

the entire substrate, this is no more the case after the sample is exposed to the larger fluence of 1.2×10^{19} ions/m^2. Stripes of bare Ir(111) are present which are shaded blue in Fig. 4(c) for better visibility. They result from vacancies that were not incorporated to the vacancy clusters located in the valleys, but migrated through the perforated h-BN layer on the order of 100 nm to form these extended vacancy islands in the form of stripes. The area of these islands as function of ion fluence is plotted in Fig. 4(a) as blue squares and specified on the right y axis. It is apparent that the islands do not form instantaneously with the onset of ion exposure, but only when n approaches saturation.

The specific stripe shape of the large vacancy islands can well be understood considering the domain structure of h-BN on Ir(111). On the sixfold-symmetric Ir(111) surface layer a threefold-symmetric monolayer of h-BN nucleates in two types of domains, each typically of triangular shape [18]. Upon layer completion the domains merge, forming domain boundaries. Under the growth conditions used, domains display lateral dimensions in the order of 0.5 μm. It was noticed already in annealing experiments that such domain boundaries are sinks for vacancies in h-BN on Ir(111) (compare Fig. 4 of Ref. [15]). Thus, once vacancy clusters have formed in the valleys, additionally created vacancies migrate through the perforated h-BN layer on Ir(111), until they reach a domain boundary where they anneal causing the Ir surface to become uncovered. Apparently, there is a limit in the size of vacancy clusters in the valleys which prevents continuous attachment of vacancies and which causes them to be expelled from the h-BN layer towards the domain boundaries. We note that the long-range migration of vacancies to domain boundaries is evidence for substrate-assisted N vacancy diffusion in h-BN on Ir(111) mentioned above, though the precise mechanism can not be elucidated on the basis of the present data.

Making the simplifying assumption that incorporation of vacancies into valley vacancy clusters ceases for larger fluences, the slope of the fluence vs area plot in Fig. 4(a) gives at large fluences the global erosion yield $Y_{\text{h-BN}}$. It amounts to $Y_{\text{h-BN}} \approx 0.25$, i.e., 0.25 B or N atoms are removed per impinging He^+ ion. Extrapolating the slope to zero fluence enables an estimate of the atoms contained in the vacancy clusters. With the known yield one obtains an average vacancy cluster size of ≈15 vacancies.

A similar dependence on ion fluence is found for ion irradiation of Gr on Ir(111). Figure 4(d) presents the quantitative analysis and Figs. 4(e) and 4(f) two representative topographs before and after saturation of n. After saturation of n it is visible in Fig. 4(f) that also for Gr on Ir(111) large vacancy islands form that uncover the Ir(111) substrate. They result from vacancies that were not incorporated to the vacancy clusters located in the individual moiré unit cells, but migrated large distances through the perforated Gr layer. The shape of the vacancy islands is

compact and very different from the striped shape for h-BN.

Gr is a single crystal on Ir(111) and has no domain boundaries. As visible in Fig. 4(f), nearly all large vacancy islands are located where the Ir substrate has step edges. At these locations Gr is strained and contains a large concentration of point defects [36]. Thus, the large vacancy islands accepting the excess vacancies presumably nucleated heterogeneously at such defects.

Using the same reasoning as above, the Gr sputtering yield on Ir(111) for 500 eV He^+ is estimated to be $Y_{Gr} \approx 0.33$. Extrapolating the slope of the fluence vs vacancy island area curve in Figs. 4(d) to zero fluence yields as an estimate for the average cluster size in the array ≈12 vacancies. We note that in Figs. 4(c) and 4(f) pronounced bright bumps are visible. They are due to accumulation of He in blisters between the 2D layer and the Ir(111) substrate and not of significance here (compare Refs. [15,37]).

In conclusion, we observe for both 2D layers that upon saturation of the vacancy cluster number density n additionally created vacancies are expelled and either anneal at h-BN domain boundaries or at sparse vacancy islands that heterogeneously nucleate in defective Gr areas. This observation implies that vacancy clusters do not grow beyond a critical size. Single vacancies created by the ion beam are apparently able to efficiently diffuse, but unable to incorporate into existing vacancy clusters within moiré unit cells. This could be due to the buildup of an energetic barrier for vacancy incorporation into an existing cluster. Considering the high temperatures under concern, it is probably more adequate to consider free-energy differences for explanation that are related to the formation energies. One could also express this finding in terms of a size-dependent 2D vacancy vapor pressure. The vacancy vapor pressure increases sharply beyond a critical vacancy cluster size such that reevaporation becomes faster than external vacancy supply, driving the cluster back to its critical size.

For h-BN the estimated average vacancy cluster size of ≈15 vacancies corresponds reasonably well with the number of chemisorbed valley atoms. It is thus plausible that once the location of the chemisorbed valley has turned into a vacancy cluster, the addition of vacancies becomes energetically unfavorable due to the excess deformation of the layer and the more unfavorable binding to the substrate. Therefore, tentatively the size of the chemisorbed valley is identified with the size of the critical vacancy cluster. The self-limitation of growth mimics the behavior of magic clusters of atoms [38–40] or vacancies [41–43]. Such clusters display a special stability at their "magic" size. However, whether the critical vacancy cluster size on h-BN is atomically well defined or whether it depends slightly on the precise irradiation conditions remains open. Other tools than STM would be required to investigate this topic, as due to tip convolution effects STM does not provide accurate estimates of hole sizes.

For Gr the situation is similar, but less obvious. Based on previous DFT calculations [16] the growth of a vacancy cluster over the energetically disfavored top region seems to be the limiting factor. However, considering the small measured average cluster size of 12 vacancies, it could be that cluster growth beyond the high-symmetry fcc regions and hcp regions [16] is already hampered.

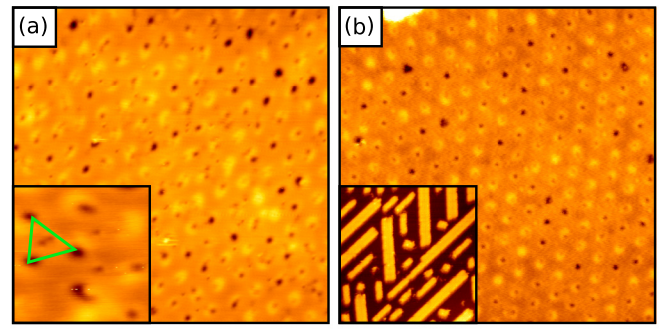

FIG. 5. (a) STM topograph of h-BN/Ir(111) after irradiation with 1.2×10^{19} ions/m^2 500 eV He^+ at 1070 K. (b) Same as (a), but irradiation at 1270 K. The inset in (b) displays an area where the h-BN layer decomposed to borophene. Image sizes are for (a) 32 nm × 32 nm, for the inset in (a) 7.5 nm × 7.5 nm, for (b) 42 nm × 42 nm, and for inset in (b) 60 nm x 60 nm. Sample bias is in (a) $U_s = +1.5$ V and for inset $U_s = +1.5$ V, and in (b) $U_s = +1.6$ V and for inset $U_s = -1.5$ V.

For both materials, h-BN and Gr, it is evident that in the regime of saturated vacancy cluster density n irradiation-induced vacancies are highly mobile, as once the deep traps are filled with vacancies the vacancies move hundreds of nanometers through the perforated 2D layer to reach domain boundaries or heterogeneously nucleated vacancy islands. The absence of a gradient in the size of the vacancy clusters, i.e., the independence of their size from the distance to the h-BN domain boundaries or to the Gr vacancy islands, underlines the large vacancy diffusion length [compare the insets of Figs. S1(b) and S1(c) as well as Figs. S2(c) and S2(d) in Ref. [35]].

D. Dependence of nanopore array formation on temperature and ion beam parameters

While for the given ion beam parameters (500 eV He^+ at normal incidence) the temperature of 1200 K appears to be suitable to create a regular nanopore array in h-BN on Ir(111), the STM topographs of Figs. 5(a) and 5(b) explore the situation at lower (1070 K) and higher (1270 K) temperature, respectively. As highlighted by the inset of Fig. 5(a), towards lower temperature the vacancies are frequently pinned at additional sites of the moiré, specifically at sites just in the center of the triangle formed by three valleys. At these locations even unirradiated samples often display defects [compare Fig. 4(a) of Ref. [44]], and it may well be that they form pinning sites for vacancies at the lower temperature. Towards higher temperature, as shown in Fig. 5(b), the vacancy cluster array is quite perfect with $n \approx 0.85$ ($n \approx 0.90$ at 1200 K). However, though rare, in some areas of the sample already thermal decomposition of the h-BN to a borophene layer is observed [compare inset of Fig. 5(b) and also Ref. [15]]. Therefore, despite the fact that vacancy cluster arrays created at 1270 K appear to be of similar quality compared to 1200-K irradiation temperature, in terms of reproducibility it seems mandatory

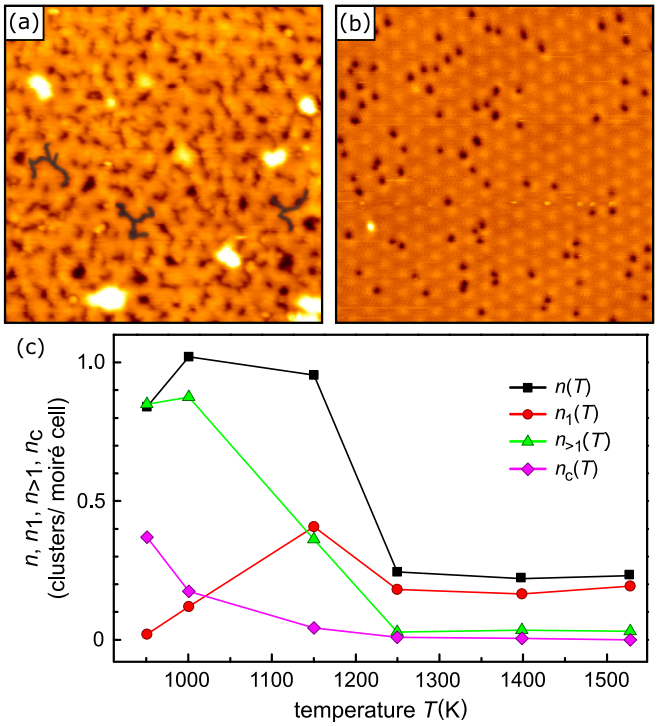

FIG. 6. (a) STM topograph of Gr/Ir(111) after irradiation with 1.2×10^{19} ions/m^2 500 eV He^+ at 950 K. A few coalesced dendritic vacancy clusters are highlighted in dark gray. (b) Same as (a), but irradiation at 1530 K. (c) Analysis of vacancy cluster number density $n(T)$ (black squares) per moiré unit cell and partial densities $n_1(T)$ (red dots, precisely one cluster per moiré unit cell), $n_{>1}(T)$ (green triangles, more than one cluster per moiré unit cell), and n_c (pink diamonds, coalesced clusters per moiré cell). Image size is 40 nm × 40 nm. Sample bias is in (a) $U_s = -2.0$ V and in (b) $U_s = -1.2$ V.

to keep a safe distance in temperature from decomposition conditions.

For Gr the situation is different as shown in Fig. 6. After irradiation at the low temperature of 950 K vacancy clusters of different moiré cells coalesce and form larger dendritic vacancy cluster aggregates, as shown in Fig. 6(a). At the very high irradiation temperature of 1530 K the number of vacancy clusters has substantially decreased compared to the situation at 1150 K already displayed in Fig. 2(a), but the vacancy clusters are still of the similar size as at 1150 K. Figure 6(c) quantifies our results. The vacancy cluster number density n (black squares) displays a pronounced drop between 1150 and 1250 K. This drop is due to a steplike reduction in nucleation probability, which reduces strongly n_1 (red dots) and $n_{>1}$ (green triangles). The broad irradiation temperature range between 1250 and 1530 K with stable vacancy cluster array properties appears ideal, if a uniform cluster size is important, though at the expense of a limited array occupation with $n \approx 0.25$. At 1150 K, n is much larger and has a maximum of cells with just one cluster (n_1, red dots), but at the expense of a few larger coalesced clusters and a substantial fraction of more than singly occupied unit cells ($n_{>1}$, green triangles).

The dependence of the formation of regular vacancy cluster arrays on h-BN/Ir(111) and Gr/Ir(111) on the ion beam parameters has not been investigated in full. Nevertheless, two key factors can be identified: (i) Trapping of the primary ions in-between the 2D layer and the metal substrate leads to blister formation and thus to detached and strained areas in the 2D layer. In this respect, He^+ irradiation is optimal, as due to the small size of the ion, its escape probability from underneath the 2D layer is highest. Even when considering the larger ion fluences needed for vacancy cluster array formation with the low sputtering yield of He^+, still using He^+ results in minimal blistering [17]. (ii) If the damage of a single impact becomes too large, already during the initial stage of vacancy cluster array formation some vacancy clusters become large and form vacancy islands. This impedes the potential for practical use of a membrane, e.g., in applications like reverse osmosis. A possible explanation for the effect is that violent impact events create large immobile vacancy clusters at wrong positions, whereby coalescence becomes more probable. Another possibility is that violent events disrupt the sheet between two vacancy clusters causing coalescence and initiating subsequent growth.

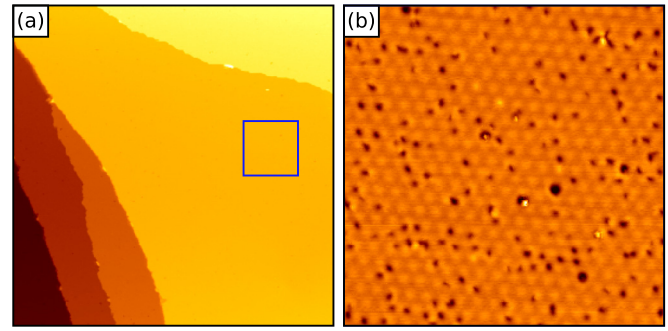

FIG. 7. (a) STM topograph of Gr/Ir(111) exposed to 3×10^{18} ions/m^2 500 eV Xe^+ at 1150 K at an angle of 75° with respect to the surface normal. Neither implanation nor large vacancy islands are apparent. Image size 355 nm × 355 nm. (b) Same as (a) with vacancy cluster resolution through magnified view. Image size 50 nm × 50 nm. For both topographs sample bias is $U_s = -1.4$ V.

An elegant alternative to normal incidence He^+ beams for vacancy cluster array fabrication is the use of Xe^+ grazing incidence irradiation. Choosing the proper grazing angle, the energy $E_\perp = E \cos^2\theta$ for the normal motion with respect to the surface can easily be tuned below the critical value for planar surface channeling E_{crit} for a given ion species [45]. Then, the ions do not penetrate the 2D layer, are reflected back to the vacuum, and do not cause violent damage through large-angle scattering events. Consequently, trapping of the primary ion species under the 2D layer is absent [17]. For 500 eV Xe^+ incident at 75° with respect to the surface normal, indeed surface channeling takes place. For these ion beam parameters $E_\perp = 33.5$ eV is still above the damage threshold $E_d \approx 20$ eV for Gr [46] and thus single vacancies are created. An example for vacancy cluster array formation without trapping is given with Fig. 7(a), where the morphology of Gr/Ir(111) after an ion fluence of 3×10^{18} ions/m^2 500 eV Xe^+ at 1150 K is shown. Neither blisters due to trapping nor large vacancy islands are visible. The absence of large vacancy islands implies that the array is still in the growth phase and not yet saturated.

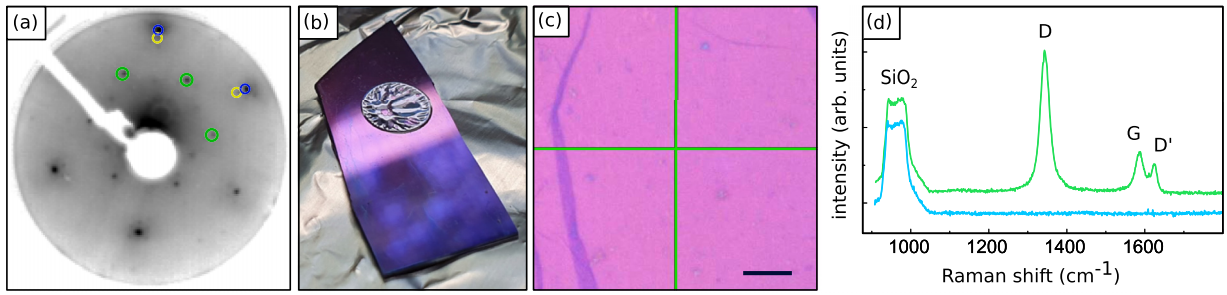

FIG. 8. Transfer of a Gr nanopore membrane that has been perforated by a fluence of 4×10^{18} ions/m^2 500 eV He^+ at 1150 K resulting in nanopore density of 1.1×10^{17} clusters/m^2. (a) 88 eV 500 eV He^+ pattern of a vacancy cluster membrane after Eu intercalation. Three $(\sqrt{3} \times \sqrt{3})$ spots of the intercalation layer are encircled green. Blue and yellow circles enclose a first-order Gr and Ir(111) spot, respectively. (b) Gr vacancy cluster membrane prior to PMMA dissolution (round) resting on an oxidized Si wafer (blue). (c) Optical microscope image of the membrane after PMMA dissolution. The scale bar is 10 μm. (d) Raman spectrum of the nanopore membrane on a Si wafer with native SiO_2 (green) acquired at the crosshair position in (c) using a using a 532-nm laser. For reference, also a spectrum of the bare wafer without membrane (blue) is plotted.

The zoom of Fig. 7(b) makes plain that the grazing incidence irradiation is indeed a viable tool for the formation of vacancy cluster arrays, though n does not reach values close to unity as obtained by 500 eV He^+ normal incidence irradiation. Since these results depend only on the presence of planar surface channeling with the condition $E_\perp < E_{crit}$ and the ability of the impinging ion to cause damage provided by $E_\perp > E_d$, other ion incidence angle and energy combinations fulfilling these conditions are expected to yield similar vacancy cluster arrays.

E. Transfer of a nanopore membrane

While uses of a vacancy cluster array resting on Ir(111) can be envisioned, e.g., as a template, for applications like filtering the detachment of the vacancy cluster membrane from Ir(111) is a prerequisite. Although the h-BN vacancy cluster membrane has a higher regularity, the membrane is likely to fall apart into μm-sized pieces due to the existence of domain boundaries. At least in principle such domain boundaries can be avoided [47] but future work is certainly needed to develop single-crystal h-BN layers. In contrast, Gr on Ir(111) exists as a high-quality single crystal and has already been successfully transferred on the mm scale as a membrane using the hydrogen bubbling method [48,49]. Therefore, here detachment of the perforated Gr membrane from Ir(111) is investigated as a first step.

Due to the strong C-Ir bonds formed by the Gr edge atoms with Ir(111) [50], a high density of small vacancy clusters increases the adhesion of the perforated Gr membrane to Ir substantially. Therefore, the plain bubbling transfer method failed in detaching of the vacancy cluster membrane from Ir(111). In order to weaken the binding of the membrane to Ir we intercalated Eu until saturation at a sample temperature of 720 K and under ultrahigh vacuum (UHV) conditions such that a $(\sqrt{3} \times \sqrt{3})$ Eu intercalation pattern forms [50] [see Fig. 8(a)]. The sample is then removed from the ultrahigh vacuum, brought to ambient conditions, coated with poly(methyl methacrylate) (PMMA), and finally immersed in a 10 % NaOH solution. The sample is then used as a cathode with a Pt counterelectrode. In a first step for 10 h an underpotential voltage of -1.4 V is applied to induce intercalation of water and its reaction with the Eu underneath Gr. Subsequently, the voltage is gradually increased above the onset of H_2 gas evolution until after 5 h and at a final voltage of -1.7 V the membrane lifts off from the substrate. The vacancy cluster membrane/PMMA disk is placed with its Gr side on an oxidized Si wafer [compare Fig. 8(b)]. After the PMMA has been dissolved, the vacancy cluster membrane is well visible in the optical microscope. Figure 8(c) displays two darker bands in the membrane which we interpret as folds created due to the transfer process.

To obtain further information on the transferred membrane, we performed Raman spectroscopy at various locations on the sample. A Raman spectrum obtained from the region in the crosshair of Fig. 8(c) is displayed in Fig. 8(d). Intense peaks associated with G mode (E_{2g} phonon) and defect activated breathing modes D and D′ are present at 1580, 1350, and 1620 cm^{-1}, correspondingly. The intensity of the defect-related D peak is about 3.5 times higher than the G peak, i.e., $I_D/I_G \approx 3.2$. Cançado *et al.* [51] related this ratio to the average defect separation L_D between ion-beam-induced defects. Based on their data, assuming similar structurally modified areas of the defects, and for the laser wavelength of 532 nm used by us, we estimate $L_D \approx 3$ nm in decent agreement with the moiré unit-cell repeat distance of 2.5 nm. The successful transfer of the membrane opens the door to future experiments characterizing and using the perforated Gr membrane.

IV. CONCLUSIONS

Formation of nanopore arrays in monolayers of h-BN and Gr through ion-induced creation of single mobile vacancies at elevated temperature is observed. For h-BN the arrays can be described as a nanopore lattice with an occupation of up to 90 % of the lattice sites. DFT demonstrates that the formation energy of a nanopore is much smaller in the chemisorbed valley compared to the surrounding mesa which agrees well with the experimentally observed location. The reason for the preference of the valley is that the dangling N and B bonds are there able to easily saturate with Ir substrate atoms without inducing additional deformation to the h-BN layer.

The average vacancy cluster size for h-BN is 15 vacancies, in decent agreement with the size of the valley containing about 20 atoms. For Gr the top region within the moiré unit cell is strongly disfavored, giving rise to preferential vacancy cluster binding in the other high-symmetry regions with an average size of about 12 vacancies. Strikingly, with increasing ion fluence the nanopores in both materials stop to grow and additionally created vacancies migrate hundreds of nanometers either to preexistent h-BN domain boundaries or to defected Gr areas, where they anneal. This finding implies an extremely strong variation of vacancy cluster formation energy as a function of position and size. Once deep traps of limited size in the moiré are filled, additional vacancies are expelled from the array of nanopores. Limiting the ion fluence to below 5×10^{18} ions/m^2 for the cases of 500 eV He^+ at normal and Xe^+ at grazing incidence results in size-limited nanopores without additional large-scale holes in the monolayer. Such membranes can be delaminated from their substrate using *in situ* intercalation to lower the h-BN or Gr binding to Ir(111) and subsequent *ex situ* application of the hydrogen bubbling method. This opens the door for the use of such dense nanopore arrays in membrane research.

ACKNOWLEDGMENTS

The project was funded by Deutsche Forschungsgemeinschaft (DFG) through Project No. MI581/22-1 ("Low energy ion irradiation of 2D materials"). B.V.S. acknowledges DFG Project No. SE 2575/4-1. N.A. acknowledges additional DFG support within CRC1238, Project No. 277146874 (subproject C01). The authors gratefully acknowledge the computing time granted by the JARA Vergabegremium and provided on the JARA Partition part of the supercomputer JURECA at Forschungszentrum Jülich.

[1] C. J. Russo and J. A. Golovchenko, Atom-by-atom nucleation and growth of graphene nanopores, Proc. Natl. Acad. Sci. USA **109**, 5953 (2012).

[2] S. C. O'Hern, M. S. H. Boutilier, J.-C. Idrobo, Y. Song, J. Kong, T. Laoui, M. Atieh, and R. Karnik, Selective ionic transport through tunable subnanometer pores in single-layer graphene membranes, Nano Lett. **14**, 1234 (2014).

[3] C. Cheng, S. A. Iyengar, and R. Karnik, Molecular size-dependent subcontinuum solvent permeation and ultrafast nanofiltration across nanoporous graphene membranes, Nat. Nanotechnol. **16**, 989 (2021).

[4] K. Celebi, J. Buchheim, R. M. Wyss, A. Droudian, P. Gasser, I. Shorubalko, J.-I. Kye, C. Lee, and H. G. Park, Ultimate permeation across atomically thin porous graphene, Science **344**, 289 (2014).

[5] J. Bai, X. Zhong, S. Jiang, Y. Huang, and X. Duan, Graphene nanomesh, Nat. Nanotechnol. **5**, 190 (2010).

[6] D. Cohen-Tanugi and J. Grossman, Water desalination across nanoporous graphene, Nano Lett. **12**, 3602 (2012).

[7] S. P. Surwade, S. N. Smirnov, I. V. Vlassiouk, R. R. Unocic, G. M. Veith, S. Dai, and S. M. Mahurin, Water desalination using nanoporous single-layer graphene, Nat. Nanotechnol. **10**, 459 (2015).

[8] Y. Yang, X. Yang, L. Liang, Y. Gao, H. Cheng, X. Li, M. Zou, R. Ma, Q. Yuan, and X. Duan, Large-area graphene-nanomesh/carbon-nanotube hybrid membranes for ionic and molecular nanofiltration, Science **364**, 1057 (2019).

[9] T. Jain, B. C. Rasera, R. J. S. Guerrero, M. S. H. Boutilier, S. C. O'Hern, J.-C. Idrobo, and R. Karnik, Heterogeneous sub-continuum ionic transport in statistically isolated graphene nanopores, Nat. Nanotechnol. **10**, 1053 (2015).

[10] L. Wang, M. S. Boutilier, P. R. Kidambi, D. Jang, N. G. Hadjiconstantinou, and R. Karnik, Fundamental transport mechanisms, fabrication and potential applications of nanoporous atomically thin membranes, Nat. Nanotechnol. **12**, 509 (2017).

[11] C. Jin, F. Lin, K. Suenaga, and S. Iijima, Fabrication of a Freestanding Boron Nitride Single Layer and Its Defect Assignments, Phys. Rev. Lett. **102**, 195505 (2009).

[12] S. M. Gilbert, G. Dunn, A. Azizi, T. Pham, B. Shevitski, E. Dimitrov, S. Liu, S. Aloni, and A. Zettl, Fabrication of subnanometer-precision nanopores in hexagonal boron nitride, Sci. Rep. **7**, 15096 (2017).

[13] H. Cun, M. Iannuzzi, A. Hemmi, J. Osterwalder, and T. Greber, Two-nanometer voids in single-layer hexagonal boron nitride, ACS Nano **8**, 7423 (2014).

[14] H. Cun, A. Hemmi, E. Miniussi, C. Bernard, B. Probst, K. Liu, D. T. L. Alexander, A. Kleibert, G. Mette, M. Weinl, M. Schreck, J. Osterwalder, A. Radenovic, and T. Greber, Centimeter-sized single-orientation monolayer hexagonal boron nitride with or without nanovoids, Nano Lett. **18**, 1205 (2018).

[15] P. Valerius, C. Herbig, M. Will, M. A. Arman, J. Knudsen, V. Caciuc, N. Atodiresei, and T. Michely, Annealing of ion-irradiated hexagonal boron nitride on Ir(111), Phys. Rev. B **96**, 235410 (2017).

[16] S. Standop, O. Lehtinen, C. Herbig, G. Lewes-Malandrakis, F. Craes, J. Kotakoski, T. Michely, A. V. Krasheninnikov, and C. Busse, Ion impacts on graphene/Ir(111): interface channeling, vacancy funnels, and a nanomesh, Nano Lett. **13**, 1948 (2013).

[17] C. Herbig, E. H. Åhlgren, and T. Michely, Blister-free ion beam patterning of supported graphene, Nanotechnology **28**, 055304 (2017).

[18] F. Farwick zum Hagen, D. Zimmermann, C. Silva, C. Schlueter, N. Atodiresei, W. Jolie, A. Martínez-Galera, D. Dombrowski, U. Schröder, M. Will *et al.*, Structure and growth of hexagonal boron nitride on Ir(111), ACS Nano **10**, 11012 (2016).

[19] A. T. N'Diaye, S. Bleikamp, P. J. Feibelman, and T. Michely, Two-Dimensional Ir Cluster Lattice on a Graphene Moiré on Ir(111), Phys. Rev. Lett. **97**, 215501 (2006).

[20] I. Horcas, R. Fernández, J. Gomez-Rodriguez, J. Colchero, J. Gómez-Herrero, and A. Baro, WSXM: a software for scanning probe microscopy and a tool for nanotechnology, Rev. Sci. Instrum. **78**, 013705 (2007).

[21] P. Hohenberg and W. Kohn, Inhomogeneous electron gas, Phys. Rev. **136**, B864 (1964).

[22] W. Kohn and L. J. Sham, Self-consistent equations including exchange and correlation effects, Phys. Rev. **140**, A1133 (1965).
[23] G. Kresse and J. Hafner, *Ab initio* molecular dynamics for liquid metals, Phys. Rev. B **47**, 558 (1993).
[24] G. Kresse and J. Furthmüller, Efficient iterative schemes for ab initio total-energy calculations using a plane-wave basis set, Phys. Rev. B **54**, 11169 (1996).
[25] G. Kresse and D. Joubert, From ultrasoft pseudopotentials to the projector augmented-wave method, Phys. Rev. B **59**, 1758 (1999).
[26] P. E. Blöchl, Projector augmented-wave method, Phys. Rev. B **50**, 17953 (1994).
[27] J. P. Perdew, K. Burke, and M. Ernzerhof, Generalized Gradient Approximation Made Simple, Phys. Rev. Lett. **77**, 3865 (1996).
[28] F. Schulz, P. Liljeroth, and A. P. Seitsonen, Benchmarking van der Waals-treated DFT: The case of hexagonal boron nitride and graphene on Ir(111), Phys. Rev. Material **3**, 084001 (2019).
[29] K. Lee, E. D. Murray, L. Kong, B. I. Lundqvist, and D. C. Langreth, Higher-accuracy van der Waals density functional, Phys. Rev. B **82**, 081101(R) (2010).
[30] I. Hamada, Van der Waals density functional made accurate, Phys. Rev. B **89**, 121103(R) (2014).
[31] K. Momma and F. Izumi, *VESTA3* for three-dimensional visualization of crystal, volumetric and morphology data, J. Appl. Crystallogr. **44**, 1272 (2011).
[32] J. Ziegler, M. Ziegler, and J. Biersack, SRIM–The stopping and range of ions in matter, Nucl. Instrum. Methods Phys. Res., Sect. B **268**, 1818 (2010).
[33] A. Zobelli, C. P. Ewels, A. Gloter, and G. Seifert, Vacancy migration in hexagonal boron nitride, Phys. Rev. B **75**, 094104 (2007).
[34] L. Weston, D. Wickramaratne, M. Mackoit, A. Alkauskas, and C. G. Van de Walle, Native point defects and impurities in hexagonal boron nitride, Phys. Rev. B **97**, 214104 (2018).
[35] See Supplemental Material at http://link.aps.org/supplemental/10.1103/PhysRevB.105.205413 for STM topographs of the fluence dependence of h-BN/Ir(111) and Gr/Ir(111), respectively, under 500 eV helium ion irradiation.
[36] J. Coraux, A. T. N'Diaye, M. Engler, C. Busse, D. Wall, N. Buckanie, F.-J. M. zu Heringdorf, R. van Gastel, B. Poelsema, and T. Michely, Growth of graphene on Ir(111), New J. Phys. **11**, 023006 (2009).
[37] C. Herbig, E. H. Åhlgren, U. A. Schröder, A. J. Martínez-Galera, M. A. Arman, J. Kotakoski, J. Knudsen, A. V. Krasheninnikov, and T. Michely, Xe irradiation of graphene on Ir(111): From trapping to blistering, Phys. Rev. B **92**, 085429 (2015).
[38] G. Schmid, The relevance of shape and size of Au_{55} clusters, Chem. Soc. Rev. **37**, 1909 (2008).
[39] H. W. Kroto, J. R. Heath, S. C. O'Brien, R. F. Curl, and R. E. Smalley, C_{60}: Buckminsterfullerene, Nature (London) **318**, 162 (1985).
[40] T. Martin, Shells of atoms, Phys. Rep. **273**, 199 (1996).
[41] D. J. Chadi and K. J. Chang, Magic numbers for vacancy aggregation in crystalline Si, Phys. Rev. B **38**, 1523 (1988).
[42] X. Y. Cui, R. K. Zheng, Z. W. Liu, L. Li, B. Delley, C. Stampfl, and S. P. Ringer, Magic numbers of nanoholes in graphene: Tunable magnetism and semiconductivity, Phys. Rev. B **84**, 125410 (2011).
[43] Sholihun, W. Amalia, D. P. Hastuti, P. Nurwantoro, A. D. Nugraheni, and R. H. Budhi, Magic vacancy-numbers in h-BN multivacancies: The first-principles study, Mater. Today Commun. **20**, 100591 (2019).
[44] M. Will, N. Atodiresei, V. Caciuc, P. Valerius, C. Herbig, and T. Michely, A monolayer of hexagonal boron nitride on Ir(111) as a template for cluster superlattices, ACS Nano **12**, 6871 (2018).
[45] H. Winter, Collisions of atoms and ions with surfaces under grazing incidence, Phys. Rep. **367**, 387 (2002).
[46] A. I. Chirita Mihaila, T. Susi, and J. Kotakoski, Influence of temperature on the displacement threshold energy in graphene, Sci. Rep. **9**, 12981 (2019).
[47] F. Orlando, P. Lacovig, L. Omiciuolo, N. G. Apostol, R. Larciprete, A. Baraldi, and S. Lizzit, Epitaxial growth of a single-domain hexagonal boron nitride monolayer, ACS Nano **8**, 12063 (2014).
[48] I. Šrut Rakić, D. Čapeta, M. Plodinec, and M. Kralj, Large-scale transfer and characterization of macroscopic periodically nanorippled graphene, Carbon **96**, 243 (2016).
[49] T. Hartl, M. Will, D. Čapeta, R. Singh, D. Scheinecker, V. Boix de la Cruz, S. Dellmann, P. Lacovig, S. Lizzit, B. V. Senkovskiy, A. Grüneis, M. Kralj, J. Knudsen, J. Kotakoski, T. Michely, and P. Bampoulis, Cluster superlattice membranes, ACS Nano **14**, 13629 (2020).
[50] P. Valerius, A. Herman, and T. Michely, Suppression of wrinkle formation in graphene on Ir(111) by high-temperature, low-energy ion irradiation, Nanotechnology **30**, 085304 (2019).
[51] L. G. Cançado, A. Jorio, E. M. Ferreira, F. Stavale, C. A. Achete, R. B. Capaz, M. V. d. O. Moutinho, A. Lombardo, T. Kulmala, and A. C. Ferrari, Quantifying defects in graphene via Raman spectroscopy at different excitation energies, Nano Lett. **11**, 3190 (2011).